Linear and cyclic amylose derivatives having brush like side groups in solution: Amylose tris(*n*-octadecylcarbamate)s

Akiyuki Ryoki [a], DongChan Kim [a], Shinichi Kitamura [b], and Ken Terao[a,]*

[a] Department of Macromolecular Science, Graduate School of Science, Osaka University, 1-1 Machikaneyama-cho, Toyonaka, Osaka 560-0043, Japan.
[b] Graduate School of Life and Environmental Sciences, Osaka Prefecture University, Gakuen-cho, Nakaku, Sakai, 599-8531, Japan.
* Corresponding author. Tel.: +81 6 6850 5459; fax: +81 6 6850 5461.
E-mail address: kterao@chem.sci.osaka-u.ac.jp

ABSTRACT
Seven linear amylose tris(*n*-octadecylcarbamate) (ATODC) samples ranging in the weight-average molar mass M_w from 2.4×10^4 to 1.5×10^6 g mol^{-1} and their seven cyclic analogues (cATODC) of which M_w are from 3.6×10^4 to 1.9×10^5 g mol^{-1} were prepared to characterize their conformation in tetrahydrohuran (THF), in 2-octanone (MHK), and in *tert*-butyl methyl ether (MTBE). Light and small-angle X-ray scattering and viscosity measurements in dilute solution were employed to determine the particle scattering function $P(q)$, the z-average mean-square radius of gyration $\langle S^2 \rangle_z$, and the intrinsic viscosity $[\eta]$. The obtained data were analyzed in terms of the wormlike chain model to determine the helix pitch per residue h and the Kuhn segment length λ^{-1} which is a measure of the chain stiffness and equal to twice the persistence length. The parameters indicate that the linear ATODC has an appreciably extended local helical structure and high chain stiffness while the latter parameter λ^{-1} in THF is lower than those for amylose alkylcarbamates with shorter side chains. This is most likely due to the repulsion between relatively long side groups. This chain extension and less stiff main chain were more significantly observed for the cyclic chains. Lyotropic liquid crystallinity in concentrated solutions supports the high rigidity of ATODC and cATODC chains in solution.

Key Words: Polysaccharide derivatives, cyclic polymers, wormlike chain, chain stiffness, hydrogen bond.

1. Introduction

Intramolecular interactions between neighboring side groups of polymers may play an important role for the conformation of polymers in solution. One of the most significant examples is molecular bottlebrushes or polymacromonomers of which main chain becomes stiffer with increasing the side chain length [1-4]. Similar finding was also reported for polymers having different alkyl side chains, that is, polymethacrylates [5, 6] and polysilanes [7, 8]. Synthetic techniques of comb-like polymers were recently extended to non-linear polymers [9, 10] such as star [11], comb [12], and cyclic [13-16] chains in order to observe their branching structure or topology by the atomic force microscopy (AFM) or to obtain novel functional materials. Solution properties of the semiflexible or rigid nonlinear polymers are however much less investigated than those for linear polymers [17-20]. Indeed, while dilute solution properties were reported for cyclic comb polymers [14, 21], conformational difference between cyclic and the corresponding linear chain were rarely discussed.

Meanwhile, we recently prepared three kinds of cyclic amylose carbamate derivatives with phenyl [22], *n*-butyl [23], and 3,5-dimethylphenyl [24] side groups from enzymatically synthesized cyclic amylose (cESA), which has substantially no linear contamination [25, 26].

If we choose appropriate isocyanate with relatively long alkyl chains, macrocyclic comb-like polymers can be synthesized from cESA. We thus prepared linear and cyclic amylose tris(*n*-octadecylcarbamate) (ATODC and cATODC, Fig. 1) from enzymatically synthesized linear amylose (ESA) and cESA, respectively. Light and small-angle X-ray scattering measurements were performed to obtain the weight-average molar mass M_w, the particle scattering function $P(q)$, the *z*-average mean square radius of gyration $\langle S^2 \rangle_z$, and the second virial coefficient A_2 to determine their conformational properties of macrocyclic comb chains in solution.

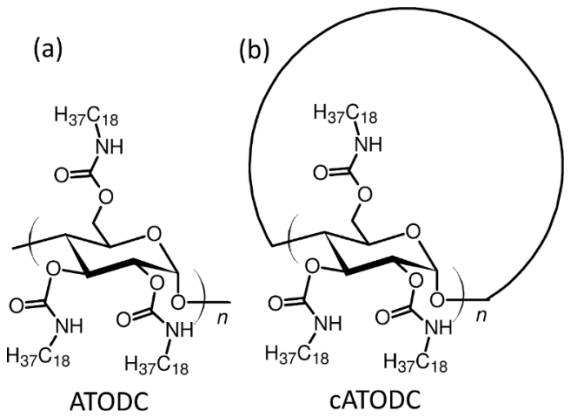

Fig. 1. Chemical structures of (a) ATODC and (b) cATODC.

Cyclic or ring polymers are much less investigated than the linear polymers owing to the difficulty to synthesize suitable model polymers. Chain conformation of cyclic DNA [17, 27], cyclic polysaccharides [26, 28, 29], polystyrene [30-35], and polydimethylsiloxane [36] were reported other than above mentioned macrocyclic comb polymers. Only cyclic DNA behaves as rather rigid ring polymers while the other cyclic macromolecules have quite flexible main chain in solution. On the contrary, cyclic amylose tris(phenylcarbamate) (cATPC) [22, 37], cyclic amylose tris(*n*-butylcarbamate) (cATBC) [23], and cyclic amylose tris(3,5-dimethylphenylcarbamate) (cADMPC) [24] have relatively high chain stiffness in solution since the corresponding linear amylose derivatives behave as semiflexible or rigid chain of which chain stiffness depends significantly on the intramolecular hydrogen bonds [38-41] (H-bonds) and/or H-bonding interactions between polymer and solvent molecules [42, 43]. A further surprising finding was that the chain stiffness and/or the local helical structure are not always the same as the corresponding linear chain [24, 37, 44]. It is however still unclear whether this topologically originated conformational difference depend on the chemical structure of the side groups.

2. Experimental section

2.1. Preparation of ATODC and cATODC samples

ATODC and cATODC samples were synthesized from five ESA and two cESA samples, respectively, in the manner reported in our previous studies [22-24, 40, 41, 43]. A typical procedure is as follows.

An ESA sample (1.69 g) and lithium chloride (3.07 g) were dried in a reaction flask under vacuum at 100 °C for 6 h. *N*,*N*-Dimethyl acetamide (40 mL) was added to dissolve them at 110 °C under argon atmosphere. Pyridine (100 mL) and *n*-octadecyl isocyanate were added to the mixture and stirred for 7 h at 105 °C. After toluene (100 mL) was added into the reaction mixture to dissolve gel-like precipitation, it was kept at 105 °C overnight. The resultant brown viscous solution was poured into excess amount of methanol to precipitate

the crude sample. It was further purified by successive reprecipitation using THF or toluene as a solvent and methanol or acetone as a precipitant.

The samples thus obtained were divided into several fractions by means of the fractional precipitation with THF and methanol as the solvent and the precipitant, respectively. Appropriate fractions, seven ATODC and seven cATODC samples, were used in this study.

^{1}H NMR, infrared (IR) absorption, and elemental analysis measurements were performed for the all samples to confirm the chemical structure in the same manner as reported previously [40]. The obtained weight ratio w_N/w_C of nitrogen to carbon ranges between 0.056 and 0.060, which is similar to that for the theoretical value (0.056). The NMR and IR charts are illustrated in the supporting information. Substantially the same signals for all samples support the full substitution. It should be noted that the degree of substitution cannot be determined properly from w_N/w_C because of the low weight fraction of nitrogen atoms comparing to those with shorter alkyl side chains [40]. While the original cESA samples were characterized by the MALDI-TOF-MS measurements to confirm substantially no linear amylose contaminant, the method cannot be applied for the cATODC samples owing to insufficiently substituent in each sample. Very high molar mass linear ATODC samples (> 10^6 g mol^{-1}) obtained from ESA, and furthermore, specific solubility only for cyclic amylose derivative supports this suggestion.

While previously investigated amylose tris(ethylcarbamate) (ATEC), amylose tris(*n*-butylcarbamate) (ATBC), and amylose tris(*n*-hexylcarbamate) (ATHC) are soluble not only in THF and chloroform but also some alcohols [41, 45], ATODC was not soluble in alcohols as shown in Table 1. We thus chose THF, 2-octanone (MHK), and *tert*-butyl methyl ether (MTBE) as solvents for the following measurements. As a preliminary experiments, we found both ATODC and cATODC form liquid crystal phase in concentrated solution, suggesting high chain stiffness in these solvent systems.

Table 1
Solubility of amylose alkylcarbamates (ATACs) at room temperature

solvent	ATEC[a]	ATBC[b]	ATHC[a]	ATODC
n-hexane	I	I	I	I
2-octanone (MHK)	I	S	S	S
tert-butyl methyl ether (MTBE)	I	S	I	S
tetrahydrofuran (THF)	S	S	S	S
chloroform	S	S	S	S
toluene	I	S	I	S
acetone	S	S	S	I
1-propanol (1PrOH)	S	S	S	I
2-propanol (2PrOH)	S	S	I	I
methanol (MeOH)	S	S	I	I

S: soluble. I: insoluble. [a] Refs. [41, 46]. [b] Refs. [40, 45, 46].

2.2. Size-exclusion chromatography with multi-angle light scattering (SEC-MALS)

SEC-MALS measurements were performed for all ATODC and cATODC samples with a DAWN DSP multi-angle light scattering photometer and a refractive index detector in a JASCO GPC-900 liquid chromatography system to determine M_w, the dispersity index $Đ$, and $\langle S^2 \rangle_z$ in THF at 25 °C; note that $Đ$ is defined as the ratio of M_w to the number-average molar mass M_n. A TSKguardcolumn HXL-H column and a TSKgel HXL column were connected in series. A sample loop with 100 μL was used, the flow rate was set to be 0.5 mL min^{-1}, the polymer mass concentration c of the injected solution was chosen to be between 4×10^{-4} and 3×10^{-3} g cm^{-3}, and the temperature of the column oven was set to be 40 °C. The scattering intensity at different scattering angles were recorded as a function of the elusion volume V_E. The refractive index increment $\partial n/\partial c$ (at a constant chemical potential) at the wavelength λ_0 in vacuum of the light scattering photometer (λ_0 = 633 nm) was determined to be 0.0790 cm^3 g^{-1} for **ATODC852K** with a Shultz-Cantow type differential refractometer. Molar masses were calculated taking into account A_2 estimated from SAXS measurements as described below. Note that the M_w value was underestimated about 0.4 – 3 % when A_2 was ignored. The obtained M_w and $Đ$ values are listed in Table 2.

Table 2
Weight-average molar mass M_w and dispersity index $Đ$ ($\equiv M_w/M_n$) of ATODC or cATODC samples

sample	M_w (kg mol^{-1})	$Đ$
ATODC25K	24.6	1.08
ATODC38K	37.7	1.08
ATODC102K	102	1.10
ATODC164K	164	1.18
ATODC284K	284	1.32
ATODC852K	852	1.51
ATODC1510K	1510	1.47
cATODC36K	36.1	1.16
cATODC55K	54.7	1.09
cATODC74K	74.2	1.07
cATODC77K	77.1	1.15
cATODC115K	115	1.10
cATODC122K	122	1.22
cATODC191K	191	1.15

2.3. Small angle X-ray scattering (SAXS) measurements

SAXS measurements were performed at the BL-10C (or BL-6A for preliminary measurements) beamlines in KEK-PF (Ibaraki, Japan) and at the BL40B2 beamline in SPring-8 (Hyogo, Japan) for all ATODC and cATODC samples in THF, in MTBE, and in MHK at 25 °C to determine $P(q)$ and $\langle S^2 \rangle_z$ except for some high M_w samples of ATODC. The camera length, λ_0, the irradiation time, and the detector were chosen to be 2.0 – 3.0 m, 0.10 – 0.15 nm, 180 – 300 s, and a Dectris PILATUS2M silicon pixel detector in KEK-PF. Those in SPring-8 were chosen to be 4.0 m, 0.10 nm, 180 – 300 s, and a Rigaku R-AXIS VII imaging plate. The beam center and the accurate camera length were determined from the Bragg reflection of silver behenate. The scattering intensity data were corrected for the incident-light intensity and the transmittance of the solution by using the ion chamber installed upper and lower ends of the capillary. A circular-average procedure was employed for each two-dimensional intensity data to obtain the scattering intensity $I(q)$ as a function of

the magnitude q of the scattering vector. Solvent and solutions with four or three different polymer mass concentrations c in which the range from 1×10^{-3} to 2×10^{-2} g cm^{-3} were measured using exactly the same capillary to obtain the excess scattering intensity $\Delta I(q)$ from the solute. The obtained $\Delta I(q)$ for ATODC were extrapolated to infinite dilution by means of the Zimm plot to determine $[c/\Delta I(q)]_{c=0}$. The resultant $[c/\Delta I(q)]_{c=0}$ data were further extrapolated to $q^2 = 0$ with the Berry plot to determine $P(q)$ and $\langle S^2 \rangle_z$ (Fig. S1 in the Supplementary Material). It should be noted that the data in THF were more fluctuated owing to the lower electron density contrast than those in the other two solvents. Similarly, the $\Delta I(q)$ data for cATODC were analyzed by means of the Guinier plot to obtain $P(q)$ and $\langle S^2 \rangle_z$ (Fig. S2 in the Supplementary Material). The A_2 data in the three solvents were also evaluated by means of the method reported elsewhere [47] to be $5 \times 10^{-5} - 4 \times 10^{-4}$ mol cm^3 g^{-2} for ATODC and $5 \times 10^{-5} - 3 \times 10^{-4}$ mol cm^3 g^{-2} for cATODC, indicating these are good solvents both for ATODC and cATODC at 25 °C.

2.4. Viscometry

Solvent and solution viscosity measurements were made for **ATODC25K**, **ATODC38K**, **ATODC102K**, **ATODC164K**, **ATODC852K**, and **ATODC1510K** in THF, MTBE, and MHK at 25 °C by using Ubbelohde type viscometers. The intrinsic viscosity $[\eta]$ and the Huggins constant k' were determined from the Huggins plot, the Fuoss-Mead plot, and the Billmeyer plot. The obtained k' values were 0.35 − 0.78 in MHK, 0.36 − 0.86 in MTBE and 0.38 − 0.69 in THF. This result is consistent with the above mentioned A_2. The measurements were not carried out for cATODC samples due to the limitation of sample quantity.

2.5. Infrared (IR) absorption spectroscopy

IR absorption spectra were recorded for **ATODC164K**, **cATODC36K**, and **cATODC191K** in MTBE and THF at 25 °C with a FT/IR-4200 (JASCO) spectrometer and a solution cell made of CaF_2 of which path length was 0.05 mm ($c \sim 0.03$ g cm^{-3}). We note that MHK is not a suitable solvent to detect H-bonding of the carbamate groups because of the significant absorption of the solvent at the corresponding wavelength.

3. Results

3.1. Dimensional and hydrodynamic properties in solution

Double logarithmic plots of $\langle S^2 \rangle_z^{1/2}$ against M_w are shown in Fig. 2. Data points for ATODC in the low M_w range obey a straight line with a slope of 0.85 – 0.95 and the slope for ATODC in THF decreases with increasing M_w. This is a typical behavior of semi-flexible polymers in solution. Data points for cATODC also drawn in the figure are appreciably smaller than those for ATODC at the same M_w. The shrinking factor g_s is defined as

$$g_s = \frac{\langle S^2 \rangle_c}{\langle S^2 \rangle_l} \tag{1}$$

where $\langle S^2 \rangle_c$ and $\langle S^2 \rangle_l$ are the gyration radius of cyclic and linear chains with the same molar mass, respectively. Except for the two lowest M_w samples, the calculated g_s values were between 0.34 and 0.51, which is substantially between $3/\pi^2$ and 1/2 for rigid and flexible rings, respectively, suggesting semiflexible nature of the higher M_w samples. The

appreciably larger g_s values for the low M_w samples are most likely due to the different local helical structure as described in the following sections.

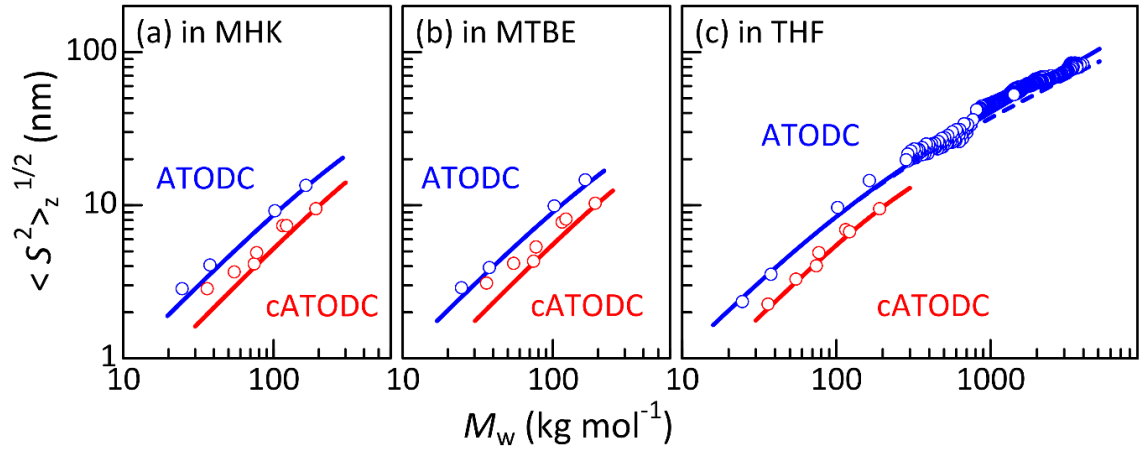

Fig. 2. Double logarithmic plots of the radius of gyration $\langle S^2 \rangle_z^{1/2}$ against M_w for ATODC (unfilled circles) and cATODC (filled circles) in MHK (a), in MTBE (b), and in THF (c) at 25 °C. Blue solid and dashed curves, theoretical values for the wormlike chains with and without the excluded-volume effect. Red solid curves, theoretical values for the wormlike rings.

The $P(q)$ data for the linear ATODC samples are illustrated in Fig. 3 in the form of the Holtzer plot. As in the case of other polysaccharide carbamate derivatives [41], the $qP(q)$ data have a plateau region between q = 0.4 – 1.9 nm^{-1} and decrease with increasing q in MHK and MTBE. This is a typical feature of the rod-like chain with finite chain thickness. An upward curvature for ATODC in THF is most likely due to the multilayered electron density profile. Indeed, similar behavior was also seen for ATBC in ethyl lactate [48] and cellulose tris(*n*-octadecylcarbamate) (CTODC) in THF [46].

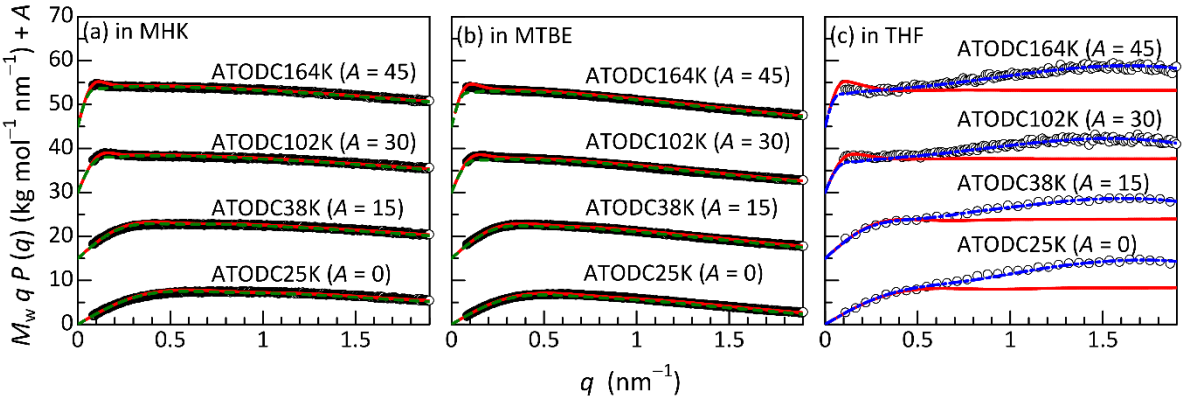

Fig. 3. Reduced Holtzer plots for ATODC in MHK (a), in MTBE (b), and in THF (c) at 25 °C. Solid red curves, theoretical values for the wormlike cylinder. Dashed green curves, theoretical values for the cylindrical rod. Dot-dashed blue curves, theoretical values of the concentric double cylinder. The ordinate values are shifted by A.

The reduced Holtzer plot was also constructed for the cATODC samples as displayed in Fig. 4. While the shape at high q region of each sample is substantially similar to that for the corresponding linear chain, a significant peak is found at the low-q range only for the cyclic chain. Similar tendency was also found for other cyclic amylose carbamates [22-24, 37].

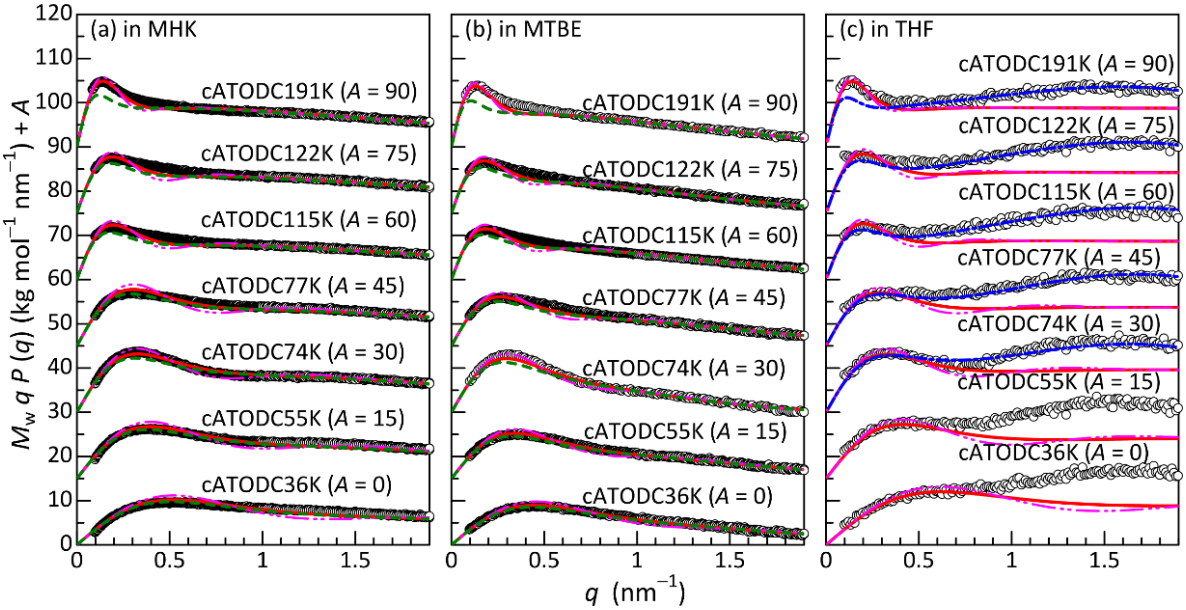

Fig. 4. Reduced Holtzer plots for cATODC in MHK (a), in MTBE (b), and in THF (c) at 25 °C. Solid red and double dot-dashed magenta curves, theoretical values for the touched-bead wormlike ring with log-normal distribution with $Đ$ = 1.20 and 1.05, respectively. Dashed green curves, theoretical values for the rigid limit with $Đ$ = 1.20. Dot-dashed blue curves, theoretical values of the concentric double cylindrical toroid with $Đ$ = 1.20. The ordinate values are shifted by A.

Molar-mass dependence of $[\eta]$ is shown in Fig. 5 for linear ATODC samples in the three solvents. The S-shaped curve with the relatively large slope is typical for rigid polymer chains.

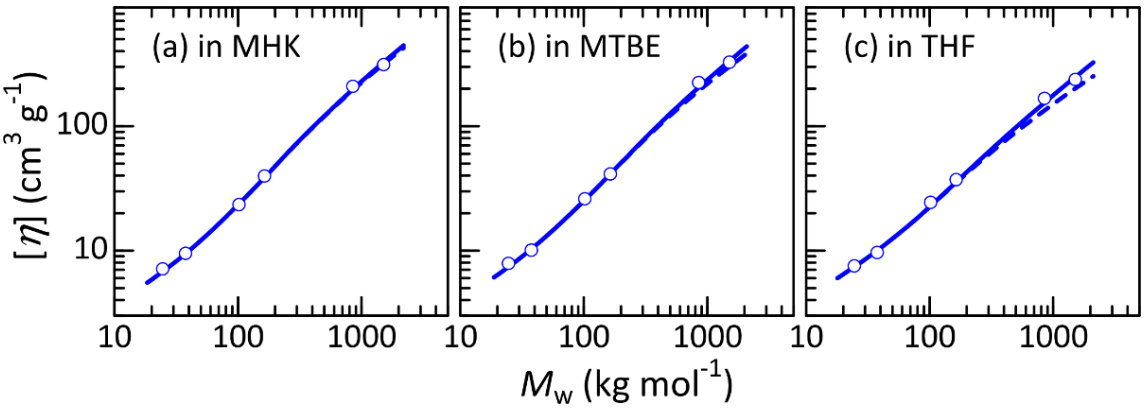

Fig. 5. Double logarithmic plots of the intrinsic viscosity $[\eta]$ against M_w for ATODC in MHK (a), in MTBE (b), and in THF (c) at 25 °C. Solid and dashed curves, theoretical values for the wormlike cylinders with and without excluded volume effects.

3.2. Solution infrared (IR) absorption spectra

The IR spectra for ATODC and cATODC in MTBE and THF are shown in Fig. 6. A split amide I band is found around 1720 cm^{-1}. The two peaks at 1740 cm^{-1} and 1700 cm^{-1} may be assigned to be free and intramolecular H-bonding C=O groups, respectively, as in the case of amylose tris(3,5-dimetylphenylcarbamate) (ADMPC) [49] and ATBC [40]. Since the observed double peak is well fitted by two Gaussian distributions, we obtained the number fraction f_{hyd} of H-bonding C=O groups for the three samples in the three solvents, that is, f_{hyd}

= 0.53 ± 0.02 for all the systems investigated. This value is the highest in the other ATAC samples in various solvents. It indicates that repulsion force between side groups are negligibly effectible to the intramolecular H-bonding of the ATODC and cATODC chains. Furthermore, the f_{hyd} value is almost independent of the solvent while those for previously investigated amylose tris(alkylcarbamate)s (ATACs) significantly depend on the solvents. This may be because currently investigated MTBE and THF do not have enough polarity to significantly break the intramolecular H-bonds.

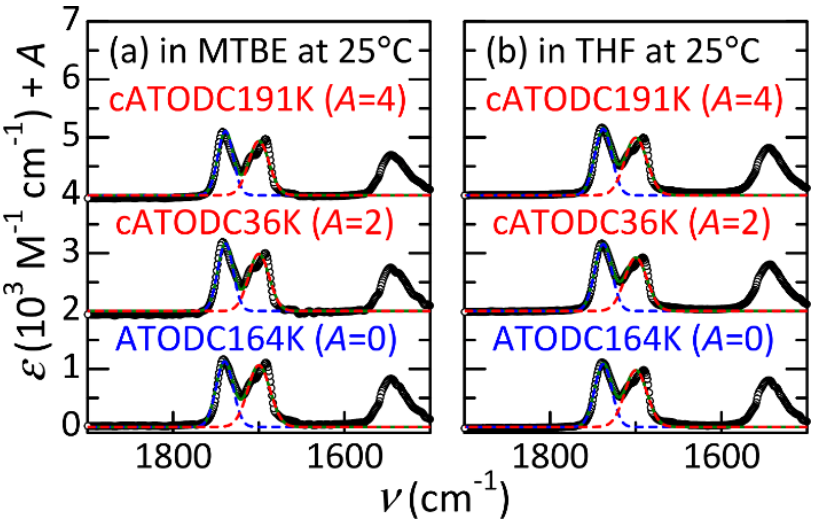

Fig. 6. Solution IR spectra for indicated samples in MTBE (a) and THF (b) at 25 °C. The ordinate values are shifted by A.

4. Discussion

4.1. Analyses in terms of the linear wormlike chain: ATODC

The particle scattering function $P(q)$ of linear wormlike chains can be calculated in terms of the Nakamura-Norisuye expression for the wormlike cylinder [50, 51]. The theoretical $P(q)$ can be calculated by their equation with the contour length L, the Kuhn segment length λ^{-1} (or twice the persistence length), and the chain diameter d. The first parameter L is proportional to M_w as follows,

$$L = \frac{hM_w}{M_0} \tag{2}$$

with M_0 being the molar mass of the repeat unit (M_0 = 1049 g mol^{-1}) and h the helix pitch (or rise) per residue. A curve fitting procedure was employed for ATODC samples in MHK and MTBE. Two parameters, h and d, were uniquely determined to be h = 0.36 nm and d = 1.5 nm in MHK and h = 0.39 nm and d = 2.3 nm in MTBE while λ^{-1} cannot be determined since the obtained theoretical values are substantially the same as the rod limiting value as illustrated in Fig. 3. If we assume the λ^{-1} value determined from [η] described below, the theoretical $P(q)$ quantitatively explains the experimental data. Upward curvature for ATODC in THF may not, however, be explained by the theory. This is most likely because the side alkyl groups have lower electron density than the core region and solvent. According to our recent study [46], experimental data for CTODC, which has the same side group as ATODC, were well fitted by the theoretical values for the concentric double cylinder, of which $P(q)$ can be expressed as [52]

$$P(q)=\int_0^{\pi/2}\left[\frac{d_o^2 G\left(q,\beta,\frac{d_o}{2},\frac{L}{2}\right)+fd_i^2 G\left(q,\beta,\frac{d_i}{2},\frac{L}{2}\right)}{d_o^2+fd_i^2}\right]^2 \sin\beta\,\mathrm{d}\beta \tag{3}$$

$$G(q,\beta,a,b)=\frac{\sin(qb\cos\beta)\,2J_1(qa\sin\beta)}{q^2 ab\sin\beta\cos\beta} \tag{4}$$

$$f=\frac{\Delta\rho_i-\Delta\rho_o}{\Delta\rho_o} \tag{5}$$

when the chain flexibility is negligible. Here, d_i and d_o are the diameter of the inner and outer cylinders, $\Delta\rho_i$ and $\Delta\rho_o$ are the corresponding excess electron densities, and J_1 is a first-order Bessel function of the first kind. We estimated h, d_i, d_o, and f to be 0.40 nm, 2.5 nm, 3.2 nm, and –2.2, respectively, to fit the experimental data as shown in Fig. 3. It should be noted that the experimental data for ATODC in MHK and MIBK may be explained by the same d_i and d_o with f = –2.9, and –6.0, respectively. The obtained theoretical values for high molar mass ATODC in THF at low q region somewhat underestimate the experimental data which can be reproduced by the thin wormlike chain when we choose λ^{-1} determined from $[\eta]$ described later (solid red curves in Fig. 3c).

Theoretical intrinsic viscosity $[\eta]_0$ formulated by Yamakawa et al. [17, 53, 54] for the wormlike cylinder can be calculated with the three parameters, L, λ^{-1}, and d. When we assume h from $P(q)$, the remaining two parameters, λ^{-1} and d, were unequivocally determined to be λ^{-1} = 45 ± 4 nm and d = 4.0 nm in MHK, λ^{-1} = 37 ± 4 nm and d = 3.9 nm in MTBE, and λ^{-1} = 30 ± 2 nm and d = 4.0 nm in THF. It should be noted that the d values are not consistent with those from $P(q)$ because $P(q)$ reflects electron density profile of the polymer chain as described above. Since the three solvent systems are good solvents, the viscosity expansion factor α_η defined as

$$\alpha_\eta^{\,3}=\frac{[\eta]}{[\eta]_0} \tag{6}$$

may not be negligible. We thus estimated α_η^3 in terms of the Barrett function [55] and the quasi-two-parameter (QTP) theory [17, 56, 57] with the parameters, that is, L, λ^{-1}, and the excluded volume strength B. When we approximately estimated the last parameter B from the above mentioned A_2 with the QTP scheme with a method as reported elsewhere [47], α_η was substantially close to unity for ATODC in MHK and MTBE in the current M_w range while the theoretical $[\eta]$ quite overestimated the data in THF. Theoretical values with somewhat smaller λ^{-1} of 24 nm reproduce the experimental data as shown in Fig. 5.

Likewise, theoretical gyration radii $\langle S^2\rangle_0$ for the unperturbed wormlike chain can be calculated from the following Benoit-Doty equation [58] as

$$\lambda^2\left\langle S^2\right\rangle_0=\frac{N_K}{6}-\frac{1}{4}+\frac{1}{4N_K}-\frac{1}{8N_K^2}\left[1-\exp\left(-2N_K\right)\right] \tag{7}$$

where N_K is the Kuhn segment number defined as $N_K \equiv \lambda L$. The gyration-radius expansion factor α_s defined as $\alpha_s^2 \equiv \langle S^2\rangle/\langle S^2\rangle_0$ with $\langle S^2\rangle$ being the gyration radius taking the excluded-

volume effects into consideration can be estimated in terms of the Domb-Barrett function [59] in the QTP scheme [17, 56, 57]. Two wormlike chain parameters, h and λ^{-1}, were uniquely determined for ATODC in THF when assuming B from A_2 as in the case of $[\eta]$. The experimental $\langle S^2\rangle_z$ data in the other two solvents can be explained by the same model with the parameters determined by $P(q)$ and $[\eta]$ while each wormlike chain parameter was infeasible to be determined unequivocally. We note that the chain thickness was negligible for $\langle S^2\rangle$ if we consider it as $\langle S^2\rangle = \langle S^2\rangle_0 + d^2/8$. The resultant parameters summarized in Table 3 are consistent with each other, indicating that the wormlike chain is a good model for ATODC in the three solvents.

Table 3
Wormlike chain parameters for linear ATODC in solution

solvent	method	h (nm)	λ^{-1} (nm)	B (nm)	d (nm)
MHK	$\langle S^2\rangle_z$	0.36[a]	45[a]	2.6 [b]	
	$P(q)$	0.36 ± 0.02	45[a]		1.5
	$[\eta]$	0.36[a]	45 ± 4	2.6 [b]	4.0
MTBE	$\langle S^2\rangle_z$	0.39[a]	37[a]	5.6 [b]	
	$P(q)$	0.39 ± 0.01	37[a]		2.2
	$[\eta]$	0.39[a]	37 ± 4	5.6 [b]	3.9
THF	$\langle S^2\rangle_z$	0.40 ± 0.03	24 ± 2	5.8 [b]	
	$P(q)$	0.40 ± 0.03	31[a]		3.2 [c]
	$[\eta]$	0.40[a]	24 ± 2	5.8 [b]	4.0

[a] Assumed. [b] Estimated from A_2 and the QTP theory (see text). [c] d_o.

4.2. Chain characteristics of linear ATODC

Table 4 summarizes the obtained wormlike chain parameters for ATODC along with previously investigated other ATACs [40, 41, 45, 48] and cellulose alkylcarbamates (CTACs) [46]. Although ATODC (alkyl side chain length n = 18) has the highest f_{hyd} in the investigated n range (2, 4, 6, and 18), the chain stiffness parameter (λ^{-1}) is appreciably smaller than those for ATBC (n = 4) and ATHC (n = 6) as also illustrated in Fig. 7, while the h value reflecting the local helical structure is longer than them. This indicates that repulsive forces between neighboring side chains of ATODC inhibit the formation of a tightly wound local helical structure. The chain stiffness is not only determined by intramolecular H-bonds but also by the difference in the local helical structure. Recently investigated CTACs seem to have similar tendency while the n dependence is less significant (Fig. 7). On the other hand, the chain stiffness of ATODC in MHK and MTBE is quite higher than that in THF while they have almost the same h value and f_{hyd} (in MTBE). Similar solvent dependent chain stiffness was also found for an amylose carbamate derivative having bulky side groups, that is, ADMPC [43] and ATPC [42], in Fig. 8 whereas the wormlike chain parameters for ATACs with shorter side groups significantly depends on f_{hyd} [40, 41, 45]. This suggests that H-bonding MHK and MTBE molecules may hinder the internal rotation of ATODC main chain. Taking into account the excellent ability of ADMPC [60, 61] (and ATPC) [62] as the chiral stationary phase, ATODC may have a potential use as the chiral separation agent.

Table 4
Values of h, λ^{-1}, and the number fraction f_{hyd} of intramolecular H-bonding C=O groups for ATACs and cellulose tris(alkylcarbamate)s (CTACs)

polymer	solvent	T (°C)	h (nm)	λ^{-1} (nm)	f_{hyd}	Ref.
ATODC	MHK	25	0.36 ± 0.02	45 ± 4		This work
ATODC	MTBE	25	0.39 ± 0.01	37 ± 4	0.55	This work
ATODC	THF	25	0.40 ± 0.03	24 ± 2	0.54	This work
ATHC	THF	25	0.29 ± 0.02	75 ± 5	0.53	[41]
ATHC	1PrOH	25	0.39 ± 0.02	30 ± 3	0.34	[41]
ATBC	THF	25	0.26 ± 0.01	75 ± 5	0.52	[40]
ATBC	$_{D}$-EL	25	0.26 ± 0.01	49 ± 4		[48]
ATBC	2BuOH	45	0.25 ± 0.01	40 ± 5	0.41	[45]
ATBC	2EE	25	0.25 ± 0.01	38 ± 4	0.39	[45]
ATBC	$_{DL}$-EL	25	0.26 ± 0.01	38 ± 3		[48]
ATBC	$_{L}$-EL	25	0.26 ± 0.01	32 ± 2		[48]
ATBC	1PrOH	40	0.28 ± 0.01	25 ± 2	0.33	[45]
ATBC	2PrOH	35	0.29 ± 0.01	20 ± 2	0.29	[45]
ATBC	MeOH	25	0.32 ± 0.01	11 ± 2	0	[40]
ATEC	THF	25	0.36 ± 0.02	33 ± 3	0.46	[41]
ATEC	$_{D}$-EL	25	0.35 ± 0.02	27 ± 2		[41]
ATEC	$_{L}$-EL	25	0.38 ± 0.02	15 ± 2		[41]
ATEC	2ME	25	0.38 ± 0.02	14 ± 2	0.26	[41]
ATEC	MeOH	25	0.38 ± 0.02	9 ± 1	0	[41]
CTODC	THF	25	0.51 ± 0.03	24 ± 1	0.40	[46]
CTBC	THF	25	0.40 ± 0.02	25 ± 1	0.44	[46]
CTEC	THF	25	0.45 ± 0.02	16.5 ± 1	0.42	[46]

2BuOH: 2-butanol. 2EE: 2-rthoxyethanol. EL: ethyl lactate. 2ME: 2-methoxyethanol. CTEC: cellulose tris(ethylcarbamate). CTBC: cellulose tris(*n*-butylcarbamate).

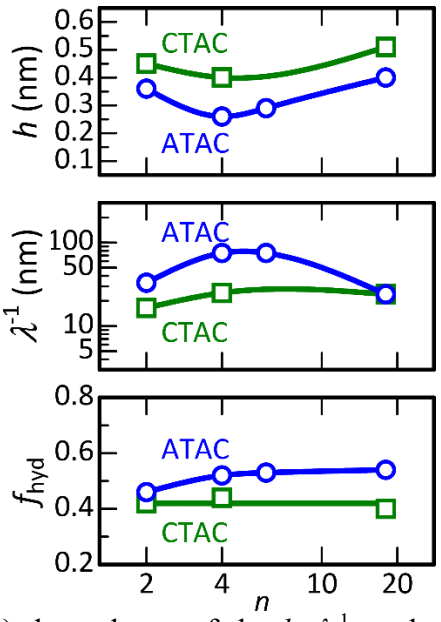

Fig. 7. Side-chain length (n) dependence of the h, λ^{-1}, and f_{hyd} for ATACs (circles) and CTACs (squares)[46] in THF.

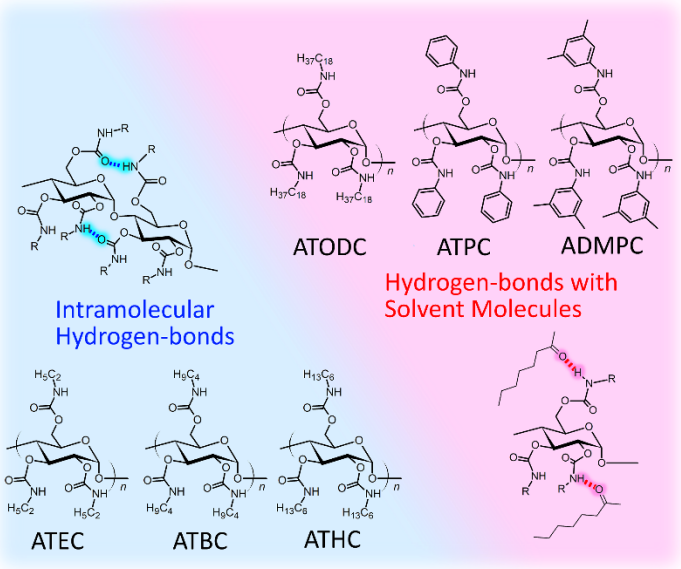

Fig. 8. Schematic representation of the origin of the chain stiffness of amylose carbamates investigated.

4.3. Analyses in terms of the cyclic wormlike chain: cATODC

According to Shimada and Yamakawa [63], gyration radii $\langle S^2\rangle_c$ of the wormlike ring may be calculated as

$$\lambda^2\langle S^2\rangle_c = \frac{N_K^2}{4\pi^2}\begin{pmatrix}1-0.1140N_K-0.0055258N_K^2\\+0.0022471N_K^3-0.00013155N_K^4\end{pmatrix} \quad for \quad N_K \le 6$$
$$= \frac{N_K}{12}\left\{1-\frac{7}{6N_K}-0.025\exp\left(-0.01N_K^2\right)\right\} \quad for \quad N_K \ge 6 \qquad (8)$$

Solid red curves in Fig. 2 are the calculated values of eq 8 with the parameters (h and λ^{-1}) for the corresponding linear ATODC listed in Table 3. They only reproduce the $\langle S^2\rangle_z$ data for

high M_w region and deviate upward with lowering M_w in MHK and in MTBE, suggesting that the wormlike chain parameters of the cyclic chain are different from those for the corresponding linear chain and/or they may depend on the chain length as depicted in our previous reports.[24, 37, 44] It should be noted that the chain thickness effect is insignificant in the M_w range investigated if we estimate it as the touched-bead model of which the contribution can be estimated as $\langle S^2\rangle = \langle S^2\rangle_c + 3d_b^2/20$ with d_b being the bead diameter estimated from the $P(q)$ described below.

Analyses of $P(q)$ allow us to determine the wormlike chain parameters for each sample. This is an effective method when the wormlike chain parameters may depend on the chain length. While $P(q)$ of the wormlike ring cannot be calculated analytically, Tsubouchi et al. [64] developed a Monte Carlo simulation method to calculate the particle scattering function $P_c(q)$ of thin wormlike ring. Furthermore, if the chain thickness is taken into account by the touched-bead model as follows,

$$P(q) = 9\left(\frac{2}{qd_b}\right)^6\left(\sin\frac{qd_b}{2} - \frac{qd_b}{2}\cos\frac{qd_b}{2}\right)^2 P_c(q) \tag{9}$$

we reported that the resultant $P(q)$ successfully reproduced the experimental data for the three amylose derivatives, that is, cATPC, cATBC, and cADMPC [24, 44]. A curve fitting procedure was examined assuming log-normal molar-mass distribution with $Đ$ = 1.05 and 1.20. The resultant theoretical values well explain the experimental data for cATODC in MHK and MTBE as illustrated in Fig. 4. While the obtained d_b values are consistent with the corresponding linear chains, that is, d_b = 1.5 ± 0.3 nm in MHK and d_b = 2.8 ± 0.6 nm in MTBE, appreciably M_w-dependent h values were evaluated. The parameter λ^{-1} was only determined for the highest M_w sample because the theoretical $P(q)$ for the wormlike ring with the corresponding λ^{-1} and lower M_w is substantially the same as those for the rigid ring.

Since the specific behavior in the $P(q)$ data for cATODC in THF cannot be analyzed by the above mentioned touched-bead model, the concentric cylindrical ring model was utilized to analyze the data for lower M_w samples. The particle scattering function $P(q)$ can be expressed as

$$P(q) = \int_0^{\pi/2}\left[\frac{d_o^2 F\left(q,\beta,\frac{d_o}{2},\frac{L}{2\pi}\right) + f d_i^2 F\left(q,\beta,\frac{d_i}{2},\frac{L}{2\pi}\right)}{d_o^2 + f d_i^2}\right]^2 \sin\beta\,\mathrm{d}\beta \tag{10}$$

$$F(q,\beta,a,b) = \frac{\int_{b-a}^{b+a} 2rJ_0(qr\sin\beta)\sin\left[q\cos\beta\sqrt{a^2-(r-b)^2}\right]dr}{\pi a^2 bq\cos\beta} \tag{11}$$

where J_0 is the Bessel function of zeroth order. This equation can be readily evaluated from the scattering function of torus [65] and the above mentioned procedure for the concentric cylinder [52] or for the concentric spheres [66]. The z-average $P(q)$ were calculated assuming log-normal distribution of L with $Đ$ = 1.20. The parameter h may uniquely be determined for five samples except for the two lowest M_w samples. This difficulty to analyse the data of the low M_w samples is probably because the length scale of the gyration radii is similar to that for the chain thickness. We note that d_i, d_o, and f were substantially the same as those for the linear chain. Assuming the obtained h value, we also attempted to estimate

λ^{-1} in terms of the thin wormlike ring to fit the data point at the low q region (see solid red curves in Fig. 4c). The parameter could only be estimated for the highest M_w sample as in the case of the other solvents systems.

To check the validity of the estimated parameters, we compared the experimental $\langle S^2 \rangle_z$ and the calculated $\langle S^2 \rangle_c$ from eq 8 with the parameters obtained for each sample in Fig. 9. Good agreement but slightly larger $\langle S^2 \rangle_z$ are most likely due to the molar mass distribution which is only considered for $P(q)$. Indeed, if we calculate the z-average values with log-normal distribution, they reproduce the experimental data almost quantitatively.

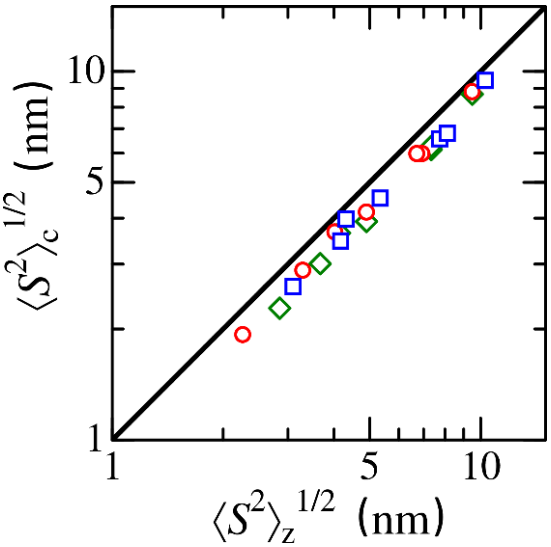

Fig. 9. Comparison between theoretical $\langle S^2 \rangle_c^{1/2}$ from eq 8 and experimental $\langle S^2 \rangle_z^{1/2}$ for cATODC in MHK (green diamonds), in MTBE (blue squares), and in THF (red circles). A solid line, $\langle S^2 \rangle_c^{1/2} = \langle S^2 \rangle_z^{1/2}$.

4.4. Comparison between cATODC and ATODC

The obtained h values for cATODC are plotted against M_w in Fig. 10. While the parameter h for the highest M_w sample is substantially the same as that in the corresponding solvent, it gradually deviates upward with decreasing M_w. This molar mass dependent crossover behavior is firstly observed in our knowledge because the molar mass range for the previously investigated cyclic amylose derivatives did not match the crossover range. While almost the same h values as that for the corresponding linear chain were obtained for the highest M_w sample, **cATODC191K**, the obtained λ^{-1} is somewhat smaller than that for the linear polymer in the same solvent, that is, $\lambda^{-1} = 25 \pm 5$ nm, 24 ± 5 nm, and 25 ± 5 nm in MHK, MTBE, and THF, respectively. Recently, we showed that the Kuhn segment number of the ring polymer becomes larger with lowering N_K for the corresponding linear chain. The current N_K data are plotted along with our recent results [24, 44] in Fig. 11. While the λ^{-1} values for cATODC tends to deviate with lowering $N_{K,linear}$, they are still fairly close to that for $N_{K,linear}$ and therefore they are fitted by the previous data for other cyclic amylose derivatives. This is reasonable because the $N_{K,linear}$ data of the current cATODC samples is higher than the previously determined threshold value of 1 – 1.5 at which the ring closure probability of the wormlike chains abruptly decreases with lowering $N_{K,linear}$ [17]. We may thus concluded that drastic conformational difference can only be observed when $N_{K,linear} < 1 – 1.5$, but it is still negligible in the higher $N_{K,linear}$ range. Even though the linear contaminant is not negligible, the 'real' h value for cATODC should be more different from the linear chain and the λ^{-1} value should be lower, indicating above mentioned conclusion may not be an artifact of contamination.

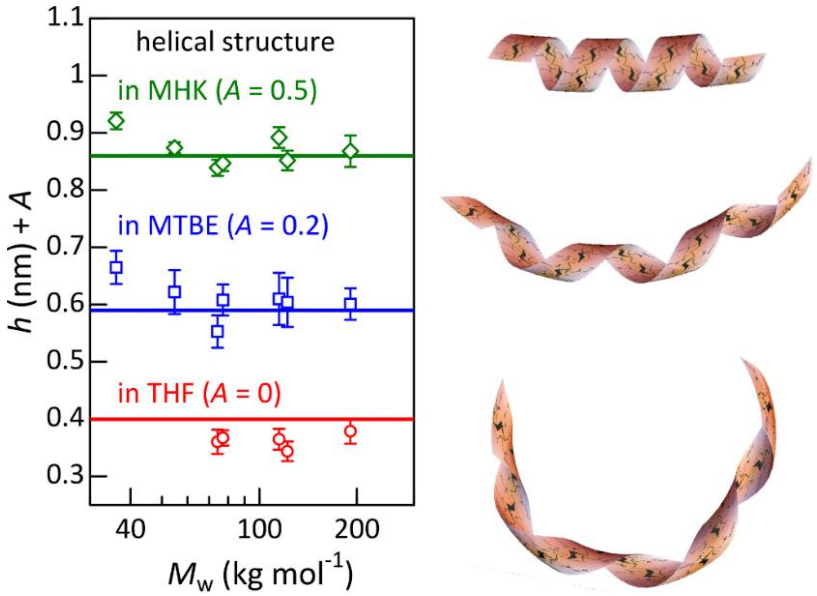

Fig. 10. Comparison of h for cATODC (symbols) with those for linear ATODC (solid lines) in MHK (green diamonds), in MTBE (blue squares), and in THF (red circles). The ordinate values are shifted by A.

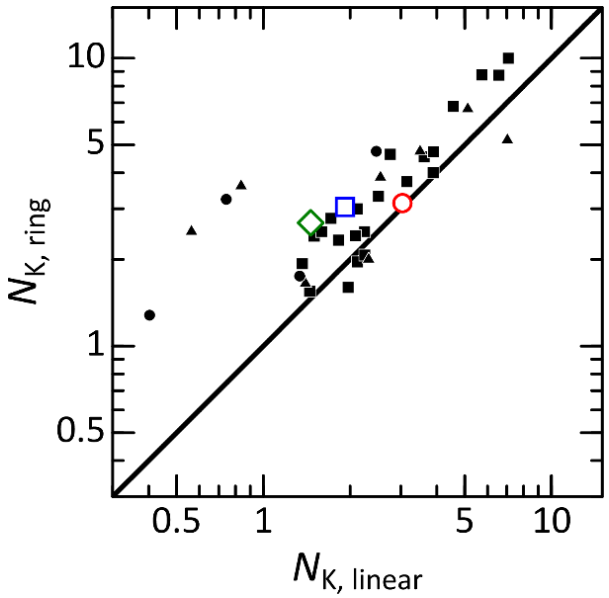

Fig. 11. Double logarithmic plots of $N_{K,ring}$ against $N_{K,linear}$ for cATODC in MHK (a green diamond), in MTBE (a blue square), and in THF (a red circle). The other symbols are the literature values[24, 44] for cADMPC (filled circles), cATPC (filled squares), and cATBC (filled triangles). A solid line, $N_{K,ring} = N_{K,linear}$.

5. Conclusion

Linear and cyclic amylose carbamate derivatives (ATODC and cATODC) having relatively long alkyl ($C_{18}H_{37}$) groups are successfully prepared from the corresponding enzymatically synthesized amylose. Chain stiffness of the linear chain is appreciably lower than those with shorter alkyl (butyl or hexyl) side chains while the main chain of many brush like polymers tends to stiffen with increasing side chain length. The alkyl side chains of ATODC mainly

extend the amylosic helix in THF and the resultant weakly wounded local helical structure retains the lower chain stiffness.

As in the case of our recent study for cyclic amylose derivatives, more extended local helical structure and somewhat less chain stiffness were observed for the cATODC samples in solution. This indicates that brush-like ring polymers may have similar behavior as those for the other semiflexible ring polymers. Both ATODC and cATODC may be good models as non-linear stiff polymers since they have good solubility in common organic solvents and indeed they form lyotropic liquid crystallinity in semi-concentrated solutions.

Acknowledgment

We are grateful to Professor Takahiro Sato (Osaka Univ.) for fruitful discussion, to Dr. Daichi Ida and Professor Takenao Yoshizaki (Kyoto Univ.) for allowing us to use the simulation program of $P(q)$, and to Dr. Noriyuki Igarashi (KEK), Dr. Nobutaka Shimizu (KEK), Dr. Noboru Ohta (SPring-8), Dr. Rintaro Takahashi (Kitakyushu Univ.), and Mr. Masaaki Kondo (Osaka Univ.) for SAXS measurements. This work was partially supported by JSPS KAKENHI Grant Nos. JP25410130 and JP17K05884. The SAXS data were acquired at the BL-10C beamline in KEK-PF under the approval of the Photon Factory Program Advisory Committee (Proposal Nos. 2013G516 and 2015G543) and at the BL40B2 beamline in SPring-8 with the approval of the Japan Synchrotron Radiation Research Institute (JASRI) (Proposal Nos. 2013B1647, 2014B1087, 2014B1715, 2015A1179, 2015B1100, 2015B1674, 2016A1053, and 2016B1088).

Appendix A. Supplementary data

Supplementary data related to this article can be found at https://doi.org/10.1016/j.polymer.2017.12.063.

References

1. Wintermantel M, Gerle M, Fischer K, Schmidt M, Wataoka I, Urakawa H, Kajiwara K, Tsukahara Y. Macromolecules 1996;29:978-83.
2. Terao K, Nakamura Y, Norisuye T. Macromolecules 1999;32:711-16.
3. Zhang B, Gröhn F, Pedersen JS, Fischer K, Schmidt M. Macromolecules 2006;39:8440-50.
4. Sugiyama M, Nakamura Y, Norisuye T. Polym J 2008;40:109-15.
5. Xu Z, Hadjichristidis N, Fetters LJ. Macromolecules 1984;17:2303-06.
6. Mays JW, Hadjichristidis N. J Macromol Sci R M C 1988;C28:371-401.
7. Kato H, Sasanuma Y, Kaito A, Tanigaki N, Tanabe Y, Kinugasa S. Macromolecules 2001;34:262-68.
8. Chung WJ, Shibaguchi H, Terao K, Fujiki M, Naito M. Macromolecules 2011;44:6568-73.
9. Sheiko SS, Sumerlin BS, Matyjaszewski K. Prog Polym Sci 2008;33:759-85.
10. Yuan J, Müller AHE, Matyjaszewski K, Sheiko SS. 6.06 - Molecular Brushes. In: Matyjaszewski K and Möller M, editors. Polymer Science: A Comprehensive Reference. Amsterdam: Elsevier, 2012. pp. 199-264.
11. Schappacher M, Deffieux A. Macromolecules 2005;38:4942-46.
12. Schappacher M, Deffieux A. Macromolecules 2005;38:7209-13.
13. Schappacher M, Deffieux A. Science 2008;319:1512-15.
14. Schappacher M, Deffieux A. J Am Chem Soc 2008;130:14684-9.
15. Xia Y, Boydston AJ, Grubbs RH. Angew Chem Int Ed 2011;50:5882-5.
16. Zhang K, Tew GN. React Funct Polym 2014;80:40-47.

17. Yamakawa H, Yoshizaki T. Helical Wormlike Chains in Polymer Solutions, 2nd ed. Berlin, Germany: Springer, 2016.
18. Norisuye T. Prog Polym Sci 1993;18:543-84.
19. Nakamura Y, Norisuye T. 2.02 - Polymer Properties in Solutions. In: Editors-in-Chief: Krzysztof M and Martin M, editors. Polymer Science: A Comprehensive Reference. Amsterdam: Elsevier, 2012. pp. 5-32.
20. Hasegawa H, Nagata Y, Terao K, Suginome M. Macromolecules 2017;50:7491-97.
21. Doi Y, Iwasa Y, Watanabe K, Nakamura M, Takano A, Takahashi Y, Matsushita Y. Macromolecules 2016;49:3109-15.
22. Terao K, Asano N, Kitamura S, Sato T. ACS Macro Lett 2012;1:1291-94.
23. Terao K, Shigeuchi K, Oyamada K, Kitamura S, Sato T. Macromolecules 2013;46:5355-62.
24. Ryoki A, Yokobatake H, Hasegawa H, Takenaka A, Ida D, Kitamura S, Terao K. Macromolecules 2017;50:4000-06.
25. Takaha T, Yanase M, Takata H, Okada S, Smith SM. J Biol Chem 1996;271:2902-08.
26. Nakata Y, Amitani K, Norisuye T, Kitamura S. Biopolymers 2003;69:508-16.
27. Bates AD, Maxwell A. DNA topology: Oxford University Press, USA, 2005.
28. Kitamura S, Isuda H, Shimada J, Takada T, Takaha T, Okada S, Mimura M, Kajiwara K. Carbohydr Res 1997;304:303-14.
29. Shimada J, Kaneko H, Takada T, Kitamura S, Kajiwara K. J Phys Chem B 2000;104:2136-47.
30. Ragnetti M, Geiser D, Hocker H, Oberthur RC. Makromol Chem Macromol Chem Phys 1985;186:1701-09.
31. Lutz P, McKenna GB, Rempp P, Strazielle C. Makromol Chem Rapid Commun 1986;7:599-605.
32. Hadziioannou G, Cotts PM, Tenbrinke G, Han CC, Lutz P, Strazielle C, Rempp P, Kovacs AJ. Macromolecules 1987;20:493-97.
33. Takano A, Ohta Y, Masuoka K, Matsubara K, Nakano T, Hieno A, Itakura M, Takahashi K, Kinugasa S, Kawaguchi D, Takahashi Y, Matsushita Y. Macromolecules 2012;45:369-73.
34. Gooßen S, Brás AR, Pyckhout-Hintzen W, Wischnewski A, Richter D, Rubinstein M, Roovers J, Lutz PJ, Jeong Y, Chang T, Vlassopoulos D. Macromolecules 2015;48:1598-605.
35. Jeong Y, Jin Y, Chang T, Uhlik F, Roovers J. Macromolecules 2017.
36. Higgins JS, Dodgson K, Semlyen JA. Polymer 1979;20:553-58.
37. Asano N, Kitamura S, Terao K. J Phys Chem B 2013;117:9576-83.
38. Bittiger H, Keilich G. Biopolymers 1969;7:539-56.
39. Burchard W. Light Scattering from Polysaccharides as Soft Materials. In: Borsali R and Pecora R, editors. Soft Matter Characterization: Springer Netherlands, 2008. pp. 463-603.
40. Terao K, Murashima M, Sano Y, Arakawa S, Kitamura S, Norisuye T. Macromolecules 2010;43:1061-68.
41. Terao K, Maeda F, Oyamada K, Ochiai T, Kitamura S, Sato T. J Phys Chem B 2012;116:12714-20.
42. Fujii T, Terao K, Tsuda M, Kitamura S, Norisuye T. Biopolymers 2009;91:729-36.
43. Tsuda M, Terao K, Nakamura Y, Kita Y, Kitamura S, Sato T. Macromolecules 2010;43:5779-84.
44. Ryoki A, Ida D, Terao K. Polym J 2017;49:633-37.
45. Sano Y, Terao K, Arakawa S, Ohtoh M, Kitamura S, Norisuye T. Polymer 2010;51:4243-48.

46. Jiang XY, Ryoki A, Terao K. Polymer 2017;112:152-58.
47. Jiang XY, Terao K, Chung WJ, Naito M. Polymer 2015;68:221-26.
48. Arakawa S, Terao K, Kitamura S, Sato T. Polym Chem 2012;3:472-78.
49. Kasat RB, Wee SY, Loh JX, Wang NH, Franses EI. Journal of chromatography B, Analytical technologies in the biomedical and life sciences 2008;875:81-92.
50. Nakamura Y, Norisuye T. J Polym Sci, Part B: Polym Phys 2004;42:1398-407.
51. Nakamura Y, Norisuye T. Brush-Like Polymers. In: Borsali R and Pecora R, editors. Soft Matter Characterization: Springer Netherlands, 2008. pp. 235-86.
52. Livsey I. Journal of the Chemical Society-Faraday Transactions Ii 1987;83:1445-52.
53. Yamakawa H, Fujii M. Macromolecules 1974;7:128-35.
54. Yamakawa H, Yoshizaki T. Macromolecules 1980;13:633-43.
55. Barrett AJ. Macromolecules 1984;17:1566-72.
56. Yamakawa H, Stockmayer WH. J Chem Phys 1972;57:2843-54.
57. Shimada J, Yamakawa H. J Chem Phys 1986;85:591-600.
58. Benoit H, Doty P. J Phys Chem 1953;57:958-63.
59. Domb C, Barrett AJ. Polymer 1976;17:179-84.
60. Okamoto Y, Aburatani R, Fukumoto T, Hatada K. Chem Lett 1987;16:1857-60.
61. Ikai T, Okamoto Y. Chem Rev 2009;109:6077-101.
62. Okamoto Y, Kawashima M, Hatada K. J Am Chem Soc 1984;106:5357-59.
63. Shimada J, Yamakawa H. Biopolymers 1988;27:657-73.
64. Tsubouchi R, Ida D, Yoshizaki T, Yamakawa H. Macromolecules 2014;47:1449-54.
65. Kawaguchi T. J Appl Crystallogr 2001;34:580-84.
66. Cebula DJ, Goodwin JW, Ottewill RH, Jenkin G, Tabony J. Colloid & Polymer Science 1983;261:555-64.